2D and 3D in-situ mechanical testing of an interpenetrating metal ceramic composite consisting of a slurry-based ceramic foam and AlSi10Mg

Joél Pascal Schukraft, Christoph Lohr, Kay A. Weidenmann

2D and 3D in-situ mechanical testing of an interpenetrating metal ceramic composite consisting of a slurry-based ceramic foam and AlSi10Mg

Joél Schukraft [a,*], Christoph Lohr [a], Kay André Weidenmann [a]

[a] Institute of Materials Resource Management, Augsburg University,
   Am Technologiezentrum 8, 86159 Augsburg.

* joel.schukraft@mrm.uni-augsburg.de

Abstract

An interpenetrating metal ceramic composite, based on a ceramic foam and an AlSi10Mg light-weight aluminum alloy, is investigated under compressive load. The ceramic preform is produced by mechanical stirring, drying and finally sintering. It has a relative density of approximately 25 % and is infiltrated via gas-pressure infiltration with the aluminum alloy. The damage processes during compressive load, as well as an understanding of crack development is in focus of this research and obtained by complementing 2D and 3D characterization methods. Therefore, a 2D surface in-situ investigation setup with an universal testing machine, a digital image correlation and a microscopy setup is used. For 3D investigation, a compression test with an in-situ X-ray computed tomography is developed and carried out to get an understanding of the material crack growth and crack propagation, as well as its failure mechanisms inside the interpenetrating metal-ceramic phase composite. The material shows crack initiations in the ceramic phase parallel to the load direction. Formation of crack clusters is followed then by a change in failure mechanism due to shear stress dominated failure with a macroscopic crack in 45 ° regarding the load direction. A good-natured failure of the composite could be determined. The combination of the 2D and 3D investigation methods gives an insight into the failure behavior of the interpenetrating composite and thus contributes to the understanding of the failure mechanism beyond the current state of knowledge.

Keywords

Interpenetrating phase composite (IPC), aluminum-alumina composite, X-ray computed tomography (CT), damage evolution, crack propagation, compression testing, in-situ investigation, digital microscopy, digital image correlation (DIC).

Introduction

Light-weight materials for structural applications under thermal load play a key role in nowadays engineering success regarding to reduction of greenhouse gases and environmentally compatible implementations in mobility and transportation [2]. An overview of strategies and different solution approaches can be found in the review article of E.G. Hertwich et al. [3].

By combining light-weight metals with ceramics, improved mechanical properties and wear resistance, as well as a higher lifetime of the composite can be achieved and the reached limits of light-weight metals can be outperformed. Such metal matrix composites (MMC) were usually produced using reinforcing ceramic particles or fibers. Industrial application like e.g. piston rings, brakes, engine blocks, connecting rods and propeller shafts [4] show the high potential of this material group.

Using an interpenetrating phase composite (IPC) instead of particles, fibers or similar discontinuous reinforcements, higher strength, stiffness and hardness, as well as wear resistance and reduced thermal expansion coefficients can be reached [5].

This is due to the hybrid microstructure of IPCs with both phases building up a complex 3D structure with two continuous constituents. By high production costs - mainly of the ceramic preform - these interpenetrating MMCs are not economically for a broad field of application yet, despite their promising mechanical properties.

By using a novel production technique, a macroscopically high homogeneous and low-cost ceramic preform can be fabricated by Morgan Advanced Materials Haldenwanger GmbH, which holds a patent on the manufacturing process [6]. The homogeneity of the preform promises reproducible and representative properties for small geometries of less than a cubic centimeter already [7], while the low production costs warrant to facilitate the transfer of bench-scale to industrial application.

The already mentioned complex interpenetrating structure makes it difficult to apply a given failure mechanism theory to the composite material. In-situ investigations are a powerful investigation method to determine damage progress and failure mechanisms. In comparison to post-mortem or ex-situ investigation, the identical sample can be used for the testing and no mechanical unloading is necessary, as there is no need to remove the specimen from the testing unit for each investigation [8].

In-situ investigations were used in a broad field of materials, as shown in excerpts for composite materials in the following. Schulz et al. investigated a metallic glass reinforced MMC with 2D in-situ scanning electron microscopy (SEM) [9], Wegner et al. used the same investigation method for an interpenetrating MMC [10], Arif et al. used in-situ SEM and micro computed tomography (μCT) on glass fiber reinforced PA66 [11], Aroush et al. investigated the damage in fiber reinforced plastics (UD quartz fibers in epoxy) via in-situ CT [12] and Saucedo-Mora et al. investigated the damage evolution in a SiC-SiC ceramic matrix composite [13].

The 3D investigation of materials via X-ray computed tomography (CT) became a popular examination method in recent years (compare e.g.[8] and [14]) as various advantages are associated with it, e.g. listed in [15]. Nevertheless, the investigation method requires complex preparation and control and expensive equipment.

To get an understanding of the mechanism of action and failure in the here investigated interpenetrating metal ceramic composite, 2D in-situ experiments as well as 3D in-situ investigations - both during compression testing - were carried out and compared to investigate the failure mechanism of the material system. The insight into the interior of the material promises to shed light on the damage processes during compressive loading, as well as an understanding of crack development. By combining 2D investigations on the surface and 3D investigations inside, an overall impression can be obtained by complementing the different characterization methods of microscopy and X-ray computed tomography.

Experimental

The interpenetrating metal-ceramic composite was manufactured of an industrial, slurry-based ceramic alumina foam, provided by Morgan Advanced Materials Haldenwanger GmbH and an AlSi10Mg cast aluminum alloy via gas pressure infiltration. The ceramic preform is heated up to 700 °C in an evacuated vacuum vessel at a residual pressure of maximum $2 \cdot 10^{-2}$ mbar with AlSi10Mg slabs. As the slabs are consequently molten and the melt surrounds the ceramic foam, an external Argon gas pressure of 40 bar is applied onto the surface of the melt bath. After a short dwell time of 10 min, the chamber is cooled down to room temperature under the remaining Argon pressure. After solidification, the infiltrated preform, i.e., the interpenetrating composite, is removed from the pressurized vessel for sample preparation. Details and schematic drawing of the process setup are described elsewhere [7].

Sample Preparation

For 2D in-situ investigation, cubed samples were cut out of an infiltrated sample block on the precision cut-off machine "Minitom" with a diamond cut-off wheel at 250 rpm under cooling with water and the cooling lubricant additive "Corrozip", each by Struers GmbH, Willich, Germany. After cutting, the samples were grinded with abrasive SiC grinding paper up to P500 to get parallel surfaces and the final size of the samples with and edge length of around 5 mm. For investigation, one surface was polished after in a four-step process, as listed in table 1. The corresponding opposite surface was coated with a speckle pattern, to investigate it with a digital image correlation (DIC) setup during testing.

For 3D in-situ investigation, cylindrical shaped samples were manufactured. Therefore, a sample slice was cut out of a sample block with a cutting machine "Servocut® 301 - MA" by Metkon, Bursa, Turkey.

With a diamond hollow drill, manufactured by Günther Diamantwerkzeuge, Idar-Oberstein, Germany and the dimensions of 3 mm as an outer diameter, cylindrical samples were cut out of the sample slice, according to the scientific exchange with B. Plank [16] or given for other materials and dimensions in Glinz et al. [17]. To reach plan parallel surfaces for compression testing, the cylinder faces were grinded parallel with abrasive SiC grinding paper of P500. The final sample size of the 3D in-situ investigated sample was a sample height of ca. 4,3 mm and a sample diameter of 1,75 mm.

2D in-situ investigation setup

For 2D in-situ investigations compression tests were carried out in a universal testing machine "1464", with a 50 kN load cell "xforceK", each by Zwick&Roell, Ulm, Germany. Interchangeable compression stamps with plane turned and then polished end faces were made of hardened machine screws of grade 12.9 with tensile strength of 1200 N/mm² and a yield strength of 1050 N/mm². Molybdenum sulfide by OKS Spezialschmierstoffe GmbH, Munich, Germany was used as a solid lubricant between the sample and the stamps in accordance to DIN 50106 [18]. A preload of 20 N was applied onto the sample, before the data logging started. The experiments were carried out travel controlled with a calculated nominal compressive strain rate of 10^{-3} 1/s. Load steps were taken at 250, 300, 340, 360 and 380 MPa. For DIC the "ARAMIS Adjustable System" with two 12 Megapixel cameras, lenses with a focal length of 100 mm and a polar filter at each lens, each by GOM, Braunschweig, Germany were used at a working distance of around 50 cm, to detect the optical strain on the sample surface with the speckle pattern throughout the whole testing process. The microstructural investigation on the polished sample surface were carried out during the load steps with a digital microscope "VHX-600" with a "VH-Z50L" optics and a magnification of 50 to 500 x, each by Keyence, Neu-Isenburg, Germany. The setup is shown in figure 1 regarding [1].

3D in-situ investigation setup

For 3D in-situ investigations compression tests were carried out in a load stage inside the X-ray computer tomograph (CT) "Phoenix nanotom 180m", by GE Sensing & Inspection Technologies GmbH, Wunstorf, Germany. The load stage, with a maximum load of 25 kN in compression or tension, was designed and constructed at the Institute of Materials Resource Management at Augsburg University and is described in detail by F. Thum et al. [19]. For compression testing of the above mentioned cylindrical composite samples, compression stamps were manufactured out of alumina rods with a diameter of 6 mm and the end faces have been polished. Regarding the investigation of the sample material, alumina suits best as compression stamp material because of the similar X-ray absorption behavior and the high hardness. The compression test is realized by a stepper motor and controlled by a LabView program, which also records the data from test (time and force-distance signal). The nominal strain rate was chosen to $1 \cdot 10^{-3}$ 1/s, analogue to the 2D-insitu tests. Load steps were taken at 235, 280, 315, 335 and 370 MPa until the maximum stress and for five more load steps at 360, 290, 240, 200 and 250 MPa. Before sample loading and at each load step CT-images were taken with a timing of 2000 ms, five averaged images at each position and 2000 positions/360 °. To prevent large displacements of the sample and associated blurring during the CT-scan, the compression stamp position was fixed after reaching the load steps and during the scan. The scan was therefore started several minutes after reaching the load step, in order to relieve stress in the material due to plastic deformation and reach a stable condition. This becomes visible in the drops of the stress-strain curve at each load step in figure 7. The X-ray beam source was powered with 80 kV voltage and 180 µA current. The focus-object distance (FOD) was 13,8 mm and the focus-detector distance (FDD) 600 mm with a resulting voxel size of (2,3 µm)³. The software components Phoenix data sx2 acquisition and Phoenix data sx2 reconstruction were used to process the data and reconstruct a 3D image of the sample, each also by GE Sensing & Inspection Technologies GmbH, Wunstorf, Germany. Further evaluations of the 3D images were carried out with the "Avizo" software by ThermoFisher Scientific, Waltham, USA. An evaluation path for crack detection was defined and is described below in "Evaluation of the X-ray CT images" in the results chapter.

Results

2D in-situ investigation results

The results of the 2D in-situ investigations are shown in figures 2, 3 and 4. The compression tests, carried out for the interpenetrating metal-ceramic composite, show a maximum stress of over 400 MPa. The load steps of the experiment for longer interruptions regarding microscopy investigations and picture capturing can be seen as load steps with small dips in the curve. After reaching the maximum stress, a decrease can be recorded. Nevertheless, the stress does not drop suddenly, like it is common for ceramic materials or composites with a brittle behavior.

The digital image correlation (DIC) data shows the strain development on the speckle pattern covered surface of the sample. Within the elastic range, a homogeneous increase in strain can be seen (figure 3), followed by a strain concentration in the center of the sample surface, parallel to the force direction. With further increase in stress, the strain locates at a weak area of the sample and forms lines of 45 degree to the direction of the force. In these areas a further increase in strain can be detected up to sample failure, introduced by cracks and followed by shear of the - by the crack divided - sample parts.

The microscopic surface investigation was carried out on the corresponding opposite surface side of the DIC investigations. Results are given for a section in figure 4 for the load steps 340, 360, 380 MPa and at the end of testing, before unloading the sample. A plastic deformation in the metallic phase can be recognized for 340 MPa and becomes more apparent at 360 MPa. A crack growth on the surface gets visible from that load step on. It links between the metallic areas and fractures the ceramic phase. In the final stage, the macroscopic crack is visible, dividing the ceramic and the metallic phase, as well as the phase boundary in the lower right corner of the image.

Evaluation of the X-ray CT images

For a lean evaluation process and optimized calculation time, the reconstructed X-ray CT images were reduced to a Region of Interest (ROI). Therefore, the Image Stack Process (ISP) of Avizo was used, to define the material section slice by slice. As it can be seen in figure 5 a), the sample volume was isolated first, to extract it from the whole 3D image where the compression stamp and beam artefacts were present (figure 5 a), second from left vs. third from left). In a further step, the region within the sample, where the material failure takes place was extracted to minimize the investigated volume to a minimum (compare ROI on fourth from left with failure of the complete sample image on the bottom, second from left). In a first analysis step, by thresholding of the grey values followed by a filtering with the function "remove of small spots" (< 5 voxel) due to incorrect grey value assignment, in the ISP process, the sample porosity was defined, as it can be seen in the right ROI-section.

For crack detection the "Brightness/Contrast" operation with "+2" in Contrast, to spread the grey values and make the automatic crack detection more unerring, was used, followed by a "Thresholding" process to binarize the image and two correction operations "remove small holes" (< 10 voxel) and "selective opening" (with a threshold of minimum two neighboring pixels to transform the pixel and four iteration steps). The selection was then inverted and masked with the above-mentioned sample volume isolated beforehand.

For better visualization of the crack and removal of the previous included residual porosity in the selection, the operation "remove small spots" was set to < 50 voxel.

To validate the process, a test was carried out to check the pore volume content in the detected crack volume. Therefore, the analyzed porosity in the unloaded sample was subtracted from the detected crack volume of the first deformed ROI. The results shown that 0,13 % of the ROI volume is residual porosity, detected as crack volume. This might be partly caused by the deformation of the sample, where a shift in volume influenced the position of porosity in the deformed sample. Also, very thin cracks, with a grey value distribution within the gray values of the material or beyond the spatial resolution could not be detected in their early stage.

The evaluation path works stabile and delivers good results for crack grow with a crack-width of > 3 voxel (dependent of the gray value), as it can be seen in figure 5 b) at "load step 8" (for corresponding stress-strain diagram compare figure 7).

3D in-situ investigation results

In figure 6, the macroscopic three-dimensional crack growth inside the sample is given, based on the evaluation path described above. At "load step 5" (for corresponding stress-strain diagram compare figure 7), it can be seen, that a little amount of porosity is visible in the images, represented by the mostly spherical shaped dots. But next to this, it can be seen, that cracks form over the whole sample ROI ("load step 5 and 6"). In further progress of the compression testing, the cracks are uniting locally and forming crack clusters, as the different colored crack clusters show in "load step 7". Preferred crack clusters, regarding the failure mechanism, are growing, while the others remain in their size or also seem to shrink (are pushed together) and a macroscopic crack forms over the whole sample diameter in a shear plane 45 degree towards load directions ("load steps 8 and 9").

For quantitative analysis different characteristics of the cracks were evaluated from the CT data. For the crack growth and the mechanism two prominent parameters were chosen and will be presented in the following. The number of detected cracks and the crack volume of the largest crack in each load step, referenced to the volume of the largest crack in "load step 9" (compare in figure 6), were compared and analyzed. The over the whole investigated sample ROI distributed cracks are very small in "load step 5", compared to the macroscopic crack in "load step 9" and the largest crack has only a relative volume of 0,08 %. The total number of cracks is around 1750 in this load step. In "load step 6" the largest crack has a volume of 0,44 % compared to the crack volume of "load step 9" and the number of cracks increases to around 2650. In "load step 7" the relative volume of the largest crack measures 4,3 %, while the number of cracks reaches 3900. In "load step 8" the macroscopic crack is clearly visible, measures 90 % of the crack volume in "load step 9" and the number of cracks levels off around 4000. For visualization, the quantitative results are given in table 2.

To get closer information about the crack initiation, a look beside the evaluation algorithm, deeper inside the material and below the limit of what is possible with automation has to be taken. Therefore, manual analysis was taken inside the material to understand the mechanisms of action and the failure of the samples, as it is shown in figure 7, where a representative crack growth inside the material succeeded. The slightly lighter gray areas represent the ceramic phase, the darker gray and round shaped areas represent the metallic phase in the 2D-section. The position of observation is marked with the black plane in the 3D image and the load step of each image is given and marked within the stress-strain diagram (each in figure 7). The observed crack starts to grow within the visibility of the resolution of the captured voxel size of $(2,3 \ \mu m)^3$ at stresses between 235 and 280 MPa within the ceramic phase at faulty or weak points or otherwise generated local stress increases. The crack continues to grow than in a plane, parallel to the force direction. A phenomenon which can also be observed, is branching of the crack, which is shown by the two different colored arrows purple and green ("load step 3"). Depending on the preferred failure direction, the crack is growing favored in one of the two crack branches. With higher loads the stepwise growing crack is visible, inside the ceramic phase or also at the phase boundary ("load step 5"). As plastic deformation sets in inside the metallic phase, the crack opens at preferred orientations. The formally with green arrows marked crack ("load step 6") seemed to vanish (it was pushed together) in favor of the purple marked one, which continued to grow instead. The crack continues to grow in the preferred direction and branches again while getting locally bridged by the metallic phase ("load step 6 and 7"). From a certain level on, the local cracks format as bigger macroscopic cracks in crack clusters, as it happens for this crack from "load step 8" on. Finally the cracks are uniting in a shear stress failure plane, as it can be seen three-dimensionally in figure 6 and a second increase in stress is recognized (stress-strain diagram figure 7).

Discussion

Crack initiation and growth theory

The failure mechanism of the composite has been investigated from crack initiation until macroscopic failure of the sample. The 3D investigations have proven, that cracks start in ceramic phase at flaw points and starts to grow in a plane, parallel to the load direction. This phenomenon is observed for brittle materials, such as alumina in detail in different publications for uniaxial compressive load. Vekinis et al. investigated alumina with defined distributed flaws [20], Wang et al. focused on the fraction theory behind and considered different models and fracture criteria [21]. Still today the question of how cracks propagate in uniaxially compressed linear brittle materials moves researchers to investigate this phenomenon [22]. Crack initiation starts not only at one specific point within the sample but within the sample volume at faulty or weak points or otherwise generated local stress increases. This microscopical and local phenomenon is also visible in the early stage of the macroscopic strain distribution on the sample surface, where concentration of strain in the vertical center of the sample is determined because of the transverse strain hindrance (see figure 3). With an increasing load the cracks continue to grow within the ceramic, at the phase boundary where local debonding of the interface due to the shrinkage of the metallic phase during solidification and cooling promotes the crack growth and in the relatively brittle intermetallic phases within the ductile metallic phase, as figure 4 shows. Especially for crack growth in the interfacial area, bridging of the crack takes place by the metallic phase, as it can be seen in figure 7 in "load step 6 and 7". In progressive load stages the cracks unite to form crack clusters in a preferred area of the sample volume, as the colored cluster and quantitative analysis show from "load step 7" on in figure 6 and table 2. Unfavorable cracks are closed and seem to vanish in the X-ray tomography images by pushed together crack flanks, which are not resolvable in the images anymore (see figure 7 in "load step 5 and 6"). At the same time the plastic deformation of the sample sets in and becomes the dominant failure mechanism, as the ceramic phase loses its mechanical strength due to the growing crack clusters. With this change in failure mechanism, also the number of cracks levels off, as it can be seen in table 2. Regarding the shear-stress-controlled failure mechanism, a shear plane is formed within the sample in a 45 ° angle towards the load direction (compare figure 6 and 7 from "load step 7" on). The sample absorbs much energy in form of plastic deformation and shows a good-natured failure while the stress is decreasing. This makes it attractive as a predictable construction material. Due to the interpenetrating morphology the sample does not fracture in different parts but remains in one peace, held by the metallic phase. A second increase in stress is recognized within the 3D in-situ investigation, which might be caused from interlocking of the crack surfaces and/or a hardening mechanism in the metallic phase [23].

As the elongation of the 3D in-situ investigation is tracked via the stepper motor rotation, the difference in strain compared to the via DIC captured strain in the 2D investigations, become obvious due to the stiffness and the play of the stage setup. Therefore, a quantitative comparison of the curves is not feasible, but for qualitative comparison, as it was intended in these studies, the stage of failure and the fracture mechanism is comparable.

From experiments with investigations on compression testing on other aluminum-alumina based (interpenetrating) materials, comparisons are made in the following:

A. Bandyopadhyay et al. [24] investigated an interpenetrating composite manufactured from a pore former process with directional hollow channels inside the ceramic, a pressure less metal infiltration and an ceramic content of 24 – 39 %. They reached a compression strength of 200 up to 480 MPa and mentioned that a finer microstructure improves the mechanical properties, as it was confirmed by Colombo et al. [25] and also the investigation of this work. Just as we could observe unto the final stage of failure, A. Bandyopadhyay et al. [24] mentioned, that the interconnected metallic network holds the fractured ceramic phase together in one piece.

H. Chang et al. [26] investigated an interpenetrating composite under high strain rate conditions (600 up to 3000 s^{-1} , based on a gel casted alumina foam with relative densities between 15 and 35 % and cell

sizes between 50 and 200 µm. As metallic phase an aluminum alloy with 8 % magnesium was used in their studies. Due to the high strain rates they reach higher stresses, strain and also deformation in the composites, but the failure of their composite also begins with ceramic cracks in the first stage, parallel to the load direction. Macroscopic debonding at the metal-ceramic interface was not observed during their investigations, which can rely on the very good interfacial bonding and/or the high strain rate. As our investigations showed local debonding, other publications mentioned the same phenomena for their investigations and also similar failure stages and mechanisms under similar testing conditions, as the following shows:

S. Roy et al. [27] investigated an aluminum-alumina composite with 35-40 % ceramic content in lamella structure and an AlSi12 aluminum alloy under compressive load and a compression rate of $1 \cdot 10^{-3}$ 1/s. They also recognized the crack starts in the ceramic phase and propagate into the metallic alloy for higher loads. Because of their anisotropic ceramic reinforcement, the cracks grow inside the ceramic phase dependent on the relative orientation between load direction and lamella orientation. Localized debonding at the metal ceramic interphases are observed, as well as in this study. That *"most of the cracks within the ceramic lamellae develop when the compressive strength of the composite is approached, suggesting that the load-bearing capacity of the ceramic has been exhausted at this point"* is a finding which can be confirmed for the interpenetrating composite, investigated here, as the transition to shear-stress-controlled failure takes place at the maximum stress, which is dominated by the metallic phase.

B. San Marchi et al. [28] investigated an interpenetrating phase composite made of a 3D-printed alumina tower with alternating 0/90 ° layers and parallel rods in each layer, infiltrated with pure aluminum. The cell size between the ceramic rods is approximately 120 µm due to the description in the paper and the ceramic content around 70 %. The compressive strength of the composite reaches 700 MPa regarding the high ceramic content. Although there is a significantly higher proportion of ceramic phase, the failure mechanism is comparable to our studies: First failures occur in the vertical ceramic rods, parallel to load direction, followed by a macroscopic shear failure of 45 ° to the loading axis.

L. Licitra et al. [29] investigated a syntactic foam of hollow sphere alumina particle and an A356 aluminum alloy at the compression rate of $1 \cdot 10^{-3}$ 1/s. They reached maximum compression strength of 250 - 275 MPa. Although the syntactic foam is different to our ceramic foam, their ceramic hollow particles with a diameter of 3 mm are much bigger than the pores of the here investigated composite and the hollow particles additionally allow a densification of the composite which appears in a plateau region in the stress-strain diagram, the qualitative microstructural failure mechanism is identical. L. Licitra et al. recognize cracks starting in the hollow sphere ceramic in direction of the load, followed by matrix deformation and finally a shear failure dominated plastic flow of the aluminum matrix combined with a shear failure, also for the brittle fracture of the alumina hollow spheres.

For the best knowledge of the authors of this publication, this is the first time, an interpenetrating metal ceramic composite is investigated with a 3D in-situ testing method in literature. The formation of three-dimensional crack cluster over the whole sample together with detailed insight to the microstructure and a quantitative crack analysis during the transition from brittle, load directed cracks to ductile failure in 45 ° towards load direction by united crack cluster was observed the first time.

Method of investigation

As the results have shown, 2D and 3D in-situ investigation are complementing each other. The 2D investigation method is an option to investigate the failure mechanism from classical testing methods [30] on, with a little modification only, because of its simple testing setup (as seen in figure 1). The image capturing is fast, compared with a whole 360 ° scan for X-ray computed tomography. Also the data size collected during one experiment is very small and efficient, compared to the required memory for a 3D scan (compare [14]). The freedom of installation space for the 2D in-situ investigation setup makes big samples and high forces possible - the maximum force is restricted by the testing machine only, which might be a multiple of the maximum of nowadays in-situ load stages. The material contrast

for the reflective surface of the aluminum metal alloy and the matt, rather light-absorbing surface of the alumina ceramic works excellent in optical microscopy, as it can be seen in figure 4. In comparison to this, the X-ray absorption of the two materials is very close due to their atomic weight and so the material contrast cannot be distinguished automated and also for the spectator it is difficult to keep the phases apart (compare figure 7). The resolution of the investigation setup is restricted by the physics behind the method. Light microscopy resolution range with the wave length of visible light [31], [32]. X-ray CTs are restricted regarding the type. The cone-beam X-ray CT used in this study is restricted by the in-situ stage tube diameter to a resolution of 2,3 µm. For the early stage of failure, the 3D in-situ investigation can detect internal failure before they become visible at the surface of the material. For surface investigation first cracks getting visible only after plastic deformation at the surface at loads of around 360 MPa, where in 3D investigation cracks can be detected at least at 280 MPa – 30 % earlier.

Thus, both methods have advantages which, when combined, lead to a versatile investigation of the failure mechanism in the interpenetrating composite: While images of the 2D investigation can only be taken during the experiments, the complete recording of the 3D structure as a stored data set by X-ray CT capturing, enables the examination and evaluation of the damage behavior of early stress levels in detail afterwards, as it can be seen in figure 6 and 7. With the 3D display of cracks, the damage formation inside the material can made visible and evaluated quantitatively (compare figure 6). The good resolution of the 2D investigation and phase differentiability makes also intermetallic phases visible and gives details about the exact crack evolution path within the different phases and the phase boundary, respectively (see figure 4).

Summary

The interpenetrating metal-ceramic composite was investigated due to its failure mechanism during compression testing. Therefor 2D as well as 3D in-situ investigation methods were used. From crack initiation on, until final macroscopic failure of the composite material, the stages of failure were detected along the stress-strain curve. Crack initiation in the ceramic phase, the crack growth within the ceramic, the interphase, as well as intermetallic phases were observed and the failure mechanism behind and the effect on the composite were discussed. A comparison with other, in literature given, aluminum-alumina composites was made and similarities in the failure process and mechanisms were identified. For the 2D and 3D investigation methods, the visibility of cracks and the mechanisms behind are compared and discussed.

Conclusion

Crack initiation starts in the composite within the ceramic phase, due to transversal contraction inhibition. Further crack growth within the ceramic, the interphase, as well as the intermetallic phases were observed and crack bridging mechanism arose at certain metallic areas. The formation of crack clusters, introducing a change in failure mechanism in the following with a shear stress dominated failure and a macroscopic crack growth in a 45 ° shear direction regarding the load could be determined and explains the remaining good-natured failure of the composite.

By combining 2D and 3D investigation methods, different effects, which are not visible with one method only, could be observed. Together the methods provide a good basic for observation and discussion of the failure effects of the material system and complement each other. To conclude - the combination of the methods provides insights into the material system that go beyond previous knowledge, contributed a decisive part to the findings and give a deeper understanding of the damage mechanism.

Outlook

For further work a correlation of acoustic emission with imaging techniques as well as simulative results for a quantitative investigation of crack initiation and crack growth will be achieved. The combination of in-situ SEM investigation with focused ion beam (FIB) preparation can give a far higher resolution than the X-ray computed tomography can realize and gives an option for crack tip investigation and the understanding of crack propagation at the phase boundary and across the phases.

Data Availability

The raw/processed data required to reproduce these findings cannot be shared at this time as the data also forms part of an ongoing study.

References

[1] Schukraft J, Lohr C, Weidenmann KA. Mechanical characterization of an interpenetrating metal-matrix composite based on highly homogeneous ceramic foams. In: Hausmann JM, Siebert M, Hehl A von, Weidenmann KA, editors. Hybrid 2020 Materials and Structures. Sankt Augustin; 2020, p. 33–39.

[2] Lewis AM, Keoleian G, Kelly J. The Potential of Lightweight Materials and Advanced Combustion Engines to Reduce Life Cycle Energy and Greenhouse Gas Emissions. In: SAE Technical Paper Series. SAE International400 Commonwealth Drive, Warrendale, PA, United States; 2014.

[3] Hertwich EG, Ali S, Ciacci L, Fishman T, Heeren N, Masanet E et al. Material efficiency strategies to reducing greenhouse gas emissions associated with buildings, vehicles, and electronics—a review. Environ. Res. Lett. 2019;14(4):43004. https://doi.org/10.1088/1748-9326/ab0fe3.

[4] Asthana R, Kumar A, Dahotre NB. Materials processing and manufacturing science. Amsterdam, Elsevier, Acad. Press; 2006.

[5] Mattern A, Huchler B, Staudenecker D, Oberacker R, Nagel A, Hoffmann MJ. Preparation of interpenetrating ceramic–metal composites. Journal of the European Ceramic Society 2004;24(12):3399–408. https://doi.org/10.1016/j.jeurceramsoc.2003.10.030.

[6] Lavrentyeva O. Verfahren zur Herstellung von aufgeschäumten keramischen Werkstoffen sowie dadurch herstellbarer keramischer Schaum: DE(DE102015202277A); 2015.

[7] Horny D, Schukraft J, Weidenmann KA, Schulz K. Numerical and Experimental Characterization of Elastic Properties of a Novel, Highly Homogeneous Interpenetrating Metal Ceramic Composite. Adv. Eng. Mater. 2020. https://doi.org/10.1002/adem.201901556.

[8] Salvo L, Suéry M, Marmottant A, Limodin N, Bernard D. 3D imaging in material science: Application of X-ray tomography. Comptes Rendus Physique 2010;11(9-10):641–9. https://doi.org/10.1016/j.crhy.2010.12.003.

[9] Schulz K, Lichtenberg K, Weidenmann KA. Discussion of the Evolution of Micro Cracks by Characterization and Modelling of Metal Matrix Composites Reinforced by Metallic Glass Particles. In: Thomsen OT, Berggreen C, Sørensen BF, editors. 20th International Conference on Composite Materials. Aalborg: Aalborg University; 2015, p. 1–12.

[10] Wegner LD, Gibson LJ. The mechanical behaviour of interpenetrating phase composites – I: modelling. International Journal of Mechanical Sciences 2000;42(5):925–42. https://doi.org/10.1016/S0020-7403(99)00025-9.

[11] Arif MF, Meraghni F, Chemisky Y, Despringre N, Robert G. In situ damage mechanisms investigation of PA66/GF30 composite: Effect of relative humidity. Composites Part B: Engineering 2014;58:487–95. https://doi.org/10.1016/j.compositesb.2013.11.001.

[12] Aroush DR-B, Maire E, Gauthier C, Youssef S, Cloetens P, Wagner HD. A study of fracture of unidirectional composites using in situ high-resolution synchrotron X-ray microtomography. Composites Science and Technology 2006;66(10):1348–53. https://doi.org/10.1016/j.compscitech.2005.09.010.

[13] Saucedo-Mora L, Lowe T, Zhao S, Lee PD, Mummery PM, Marrow TJ. In situ observation of mechanical damage within a SiC-SiC ceramic matrix composite. Journal of Nuclear Materials 2016;481:13–23. https://doi.org/10.1016/j.jnucmat.2016.09.007.

[14] Maire E, Withers PJ. Quantitative X-ray tomography. International Materials Reviews 2014;59(1):1–43. https://doi.org/10.1179/1743280413Y.0000000023.

[15] Beckmann F, Grupp R, Haibel A, Huppmann M, Nöthe M, Pyzalla A et al. In-Situ Synchrotron X-Ray Microtomography Studies of Microstructure and Damage Evolution in Engineering Materials. Adv. Eng. Mater. 2007;9(11):939–50. https://doi.org/10.1002/adem.200700254.

[16] Plank B. Sample preparation for X-ray computed tomography in-situ investigation. Wels, Austria; 2020.

[17] Glinz J, Kytýř D, Fíla T, Šleichrt J, Schrempf A, Fürst D et al. IN-SITU COMPRESSION TEST OF ARTIFICIAL BONE FOAMS IN CONTROLLED ENVIRONMENT USING X-RAY MICRO-COMPUTED TOMOGRAPHY. APP 2019;25:48–51. https://doi.org/10.14311/APP.2019.25.0048.

[18] DIN Deutsches Institut für Normung. Prüfung metallischer Werkstoffe - Druckversuche bei Raumtemperatur. 50106th ed.(DIN 50106:2016-11). Berlin: Beuth Verlag GmbH; 2016.

[19] Thum F, Potstada P, Sause MGR. Development of a 25kN In Situ Load Stage Combining X-Ray Computed Tomography and Acoustic Emission Measurement. KEM 2019;809:563–8. https://doi.org/10.4028/www.scientific.net/KEM.809.563.

[20] Vekinis G, Ashby MF, Beaumont PWR. The compressive failure of alumina containing controlled distributions of flaws. Acta Metallurgica et Materialia 1991;39(11):2583–8. https://doi.org/10.1016/0956-7151(91)90073-A.

[21] Wang EZ, Shrive NG. Brittle fracture in compression: Mechanisms, models and criteria. Engineering Fracture Mechanics 1995;52(6):1107–26. https://doi.org/10.1016/0013-7944(95)00069-8.

[22] Iskander M, Shrive N. The effect of the shape and size of initial flaws on crack propagation in uniaxially compressed linear brittle materials. Theoretical and Applied Fracture Mechanics 2020;109:102742. https://doi.org/10.1016/j.tafmec.2020.102742.

[23] Chen B, Moon SK, Yao X, Bi G, Shen J, Umeda J et al. Strength and strain hardening of a selective laser melted AlSi10Mg alloy. Scripta Materialia 2017;141:45–9. https://doi.org/10.1016/j.scriptamat.2017.07.025.

[24] Bandyopadhyay A, Atisivan R, Kuhn G, Yeruva S. Mechanical Properties of Interconnected Phase Alumina-Al Composites 24. The University of Texas at Austin; 2000.

[25] Colombo P. Macro- and micro-cellular porous ceramics from preceramic polymers. Composites Science and Technology 2003;63(16):2353–9. https://doi.org/10.1016/S0266-3538(03)00268-9.

[26] Chang H, Binner J, Higginson R, Myers P, Webb P, King G. High strain rate characteristics of 3-3 metal–ceramic interpenetrating composites. Materials Science and Engineering: A 2011;528(6):2239–45. https://doi.org/10.1016/j.msea.2010.12.016.

[27] Roy S, Butz B, Wanner A. Damage evolution and domain-level anisotropy in metal/ceramic composites exhibiting lamellar microstructures. Acta Materialia 2010;58(7):2300–12. https://doi.org/10.1016/j.actamat.2009.12.015#.

[28] San Marchi C, Kouzeli M, Rao R, Lewis JA, Dunand DC. Alumina-aluminum interpenetrating-phase composites with three-dimensional periodic architecture. Scripta Materialia 2003(49):861–6.

[29] Licitra L, Luong DD, Strbik OM, Gupta N. Dynamic properties of alumina hollow particle filled aluminum alloy A356 matrix syntactic foams. Materials & Design 2015;66:504–15. https://doi.org/10.1016/j.matdes.2014.03.041.

[30] Abramowitch S, Easley D. Introduction to Classical Mechanics. In: Biomechanics of the Female Pelvic Floor. Elsevier; 2016, p. 89–107.

[31] Abbe E. Beiträge zur Theorie des Mikroskops und der mikroskopischen Wahrnehmung. Archiv f. mikrosk. Anatomie 1873;9(1):413–68. https://doi.org/10.1007/BF02956173.

[32] Rayleigh. XV. On the theory of optical images, with special reference to the microscope. The London, Edinburgh, and Dublin Philosophical Magazine and Journal of Science 1896;42(255):167–95. https://doi.org/10.1080/14786449608620902.
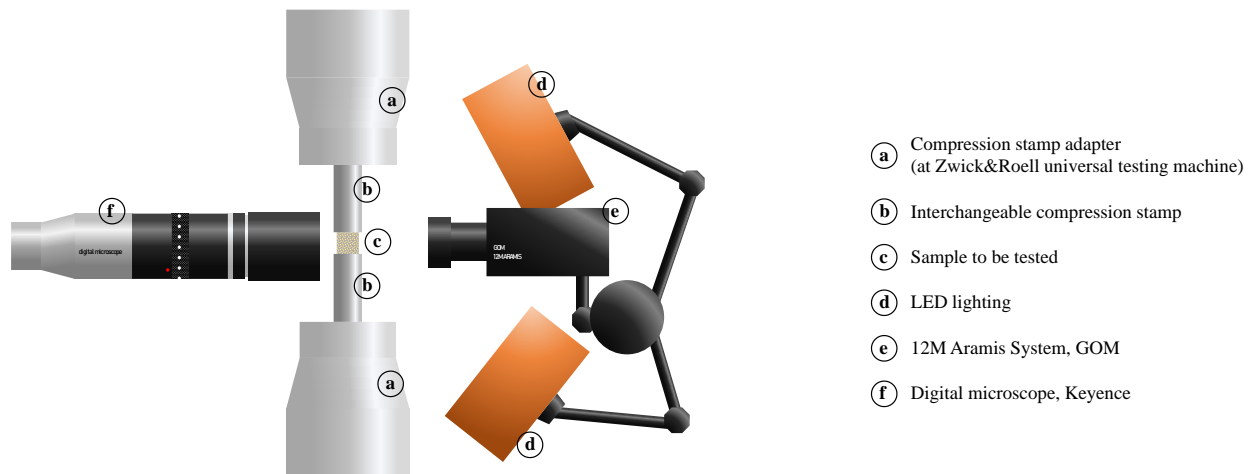
Figure 1 In-situ testing setup: Zwick&Roell universal testing machine, GOM ARAMIS Adjustable 12M System and Keyence digital microscopy [1].
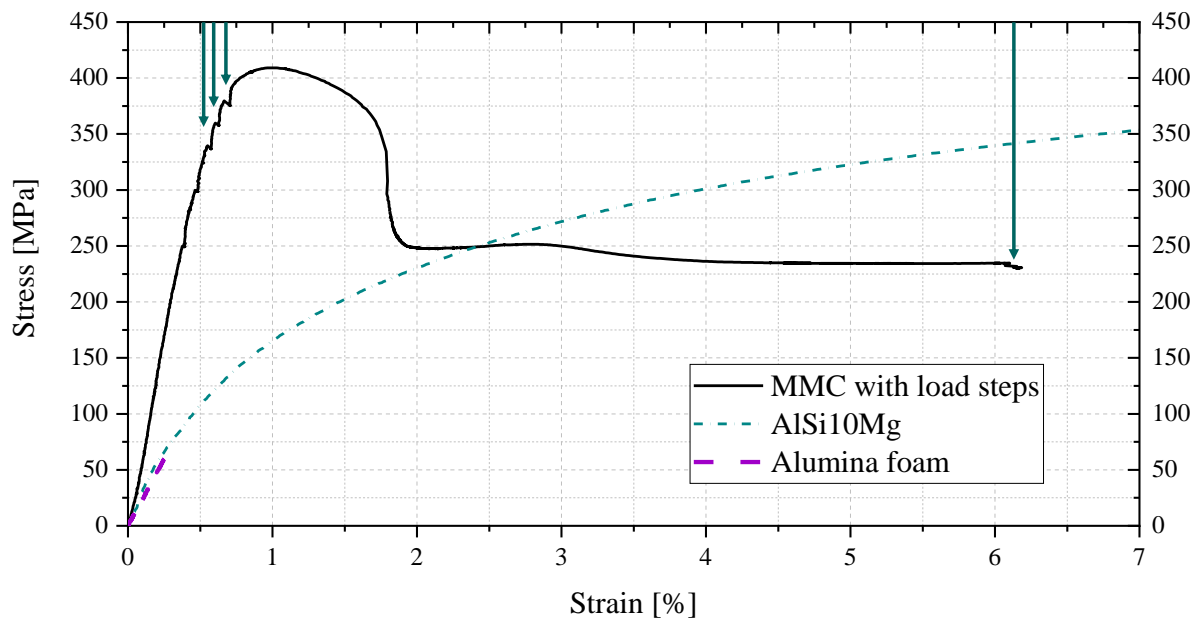

Figure 2 Stress-strain diagram of the alumina foam, the metal alloy and the composite. An increase in strength and stiffness is visible for the composite, while maintaining good natured failure. The in-situ load-steps are visible in the curve and marked with arrows for the shown micrographs.
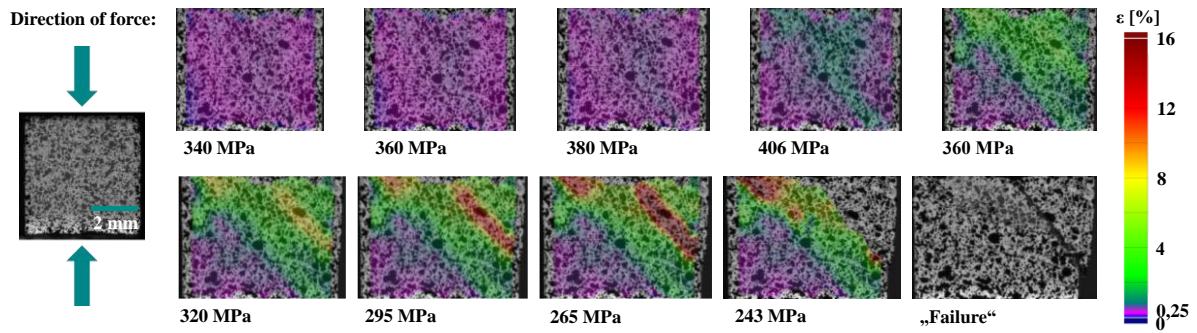
Figure 3 Strain distribution on the speckle pattern on a sample surface, captured with the digital image correlation setup for several load steps until failure of the sample. The direction of force and a scale bar is shown on the left, equal for every load step.
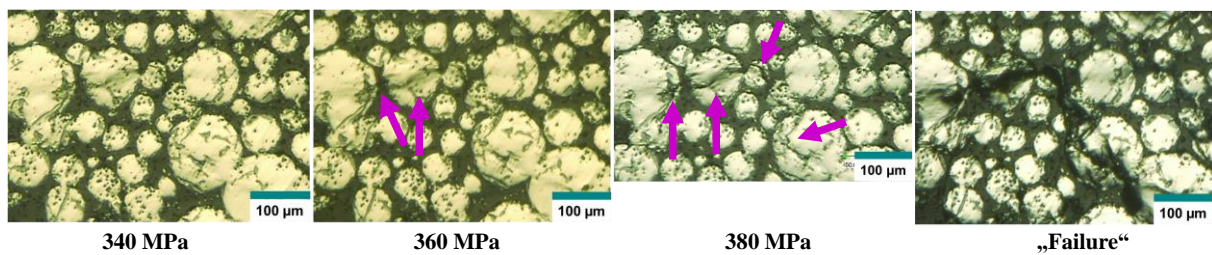

Figure 4 2D in-situ investigation of the crack formation in section at the sample surface, shown for 340, 360, 380 MPa and at the end of testing before unloading the sample (load steps are taken regarding the green arrows in figure 2). Plastic deformation and a crack in the ceramic phase get visible at 360 MPa (purple arrows). Further crack growth in the ceramic phase, plastic deformation in the metallic phase, as well as cracks along the intermetallic phases are highlighted with purple arrows at 380 MPa. [Due to manually chosen image regions on the sample surface, the load step at 380 MPa is cut in the lower section by mistake]
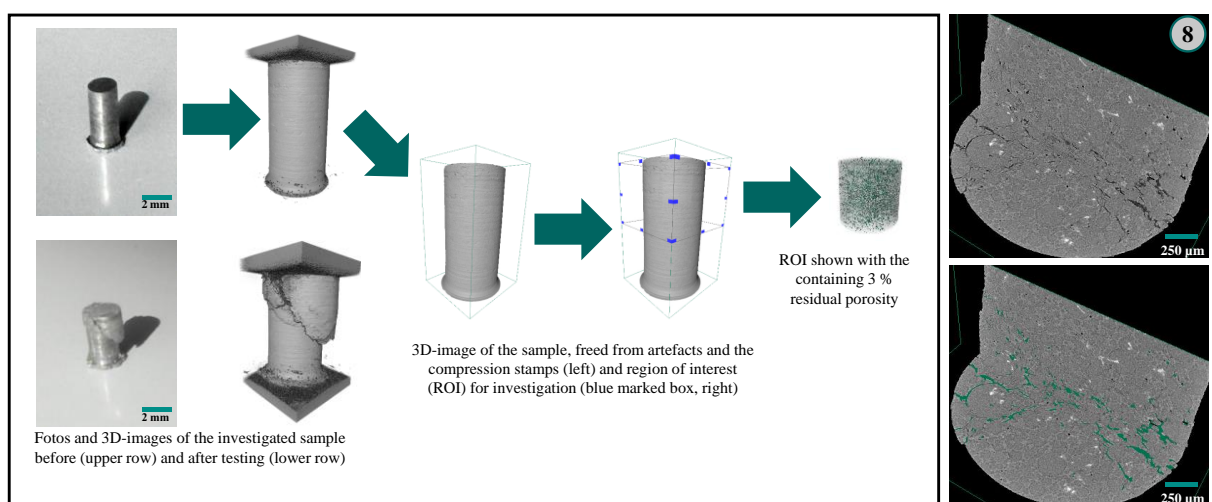

Figure 5 a) Left: Sample acquisition process of in-situ compression testing scans and reduction to an ROI. **b)** Right: Automated crack detection and quality of detection with detected crack area (green, bottom) and without (top), each at load step 8 (for corresponding stress-strain diagram see figure 7) at an excerpt of the sample volume.
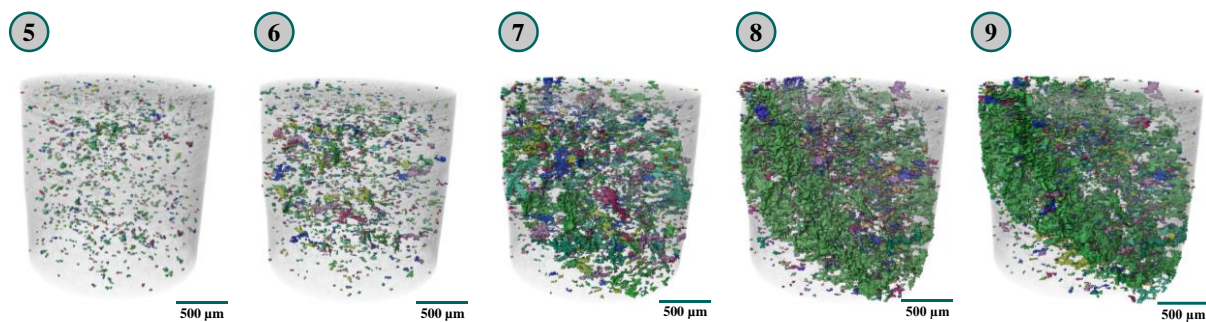
Figure 6 3D crack growth in the MMC sample analyzed with an automated crack detection from in-situ CT tests at different load steps (for corresponding stress-strain diagram compare figure 7).
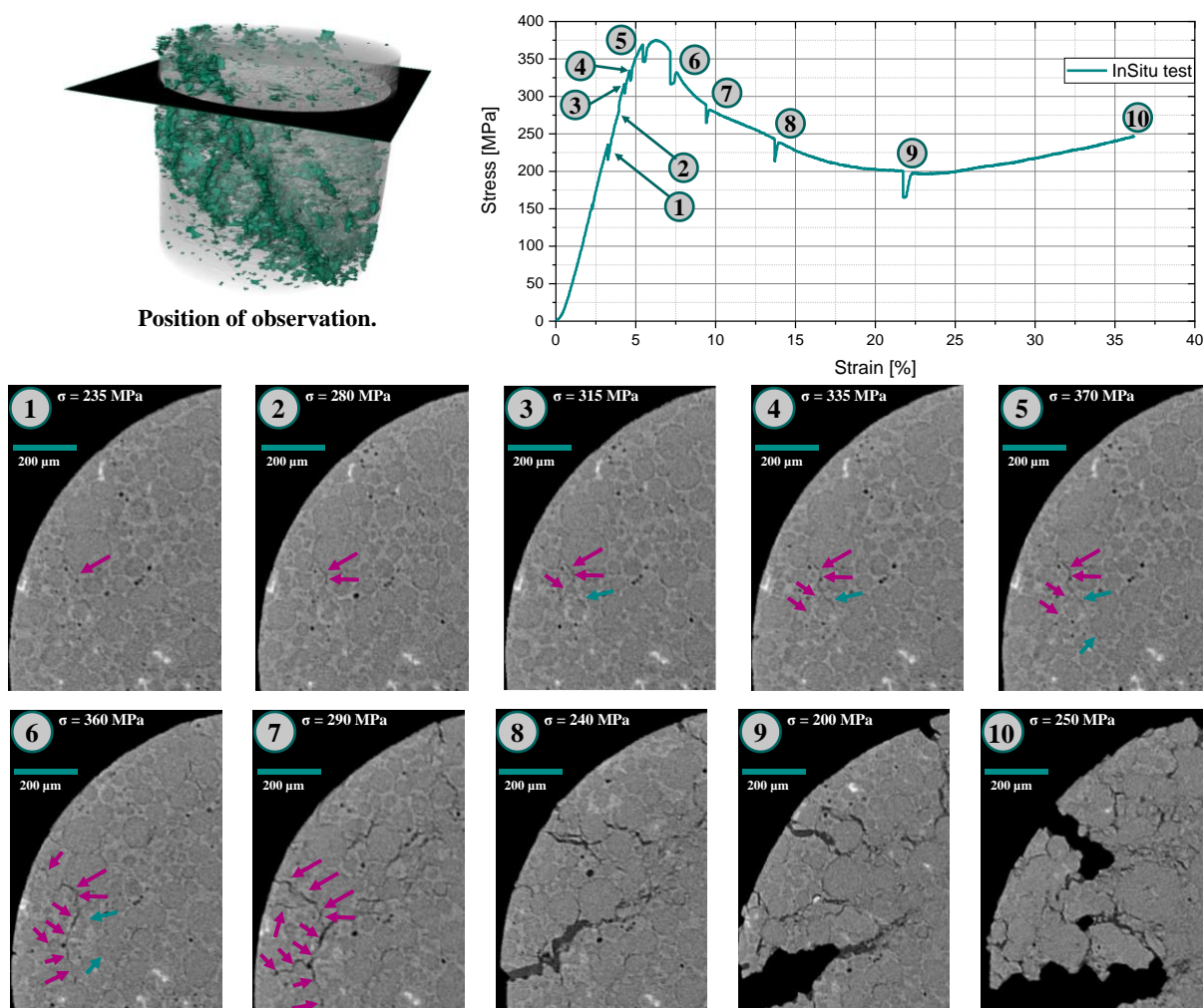

Figure 7 Top left: Position of observation marked with a black slice. Top right: Stress-strain diagram of the in-situ CT testing (also for values of figure 5 and 6) with numbers for each load step. Bottom: Step wise representation of the crack growth inside the material regarding the marked position in the top left. Each load step is marked with the corresponding number in the stress-strain diagram in the top right and the stress level.

Table 1 Polishing steps to prepare the composite specimens for microscopy.

Polishing cloth/film	Suspension	Contact pressure	Circulation	Duration
MD Largo	Diamond suspension, 9 µm	25 N	Synchronous 210/150 rpm	8 min
MD DAC	Diamond suspension, 3 µm	25 N	Synchronous 210/150 rpm	5 min
MD DUR	Diamond suspension, 1 µm	20 N	Synchronous 210/150 rpm	5 min
MD CHEM	OP-S suspension with rinse agent	15 N	Synchronous 210/150 rpm	2:30 min

Table 2 Quantitative evaluation of the crack growth in the composite material, focused on the development of crack numbers and the crack volume of the largest crack. The numbers of the load steps refer to the load steps in figure 6.

Load step		5	6	7	8	9
relative volume of the largest crack	%	0,08	0,44	4,3	90	100
number of cracks	#	1742	2634	3902	3945	4219